

Regularized Dirac delta functions for phase field models

Hyun Geun Lee and Junseok Kim^{*,†}

Department of Mathematics, Korea University, Seoul 136-701, Korea

SUMMARY

The phase field model is a highly successful computational technique for capturing the evolution and topological change of complex interfaces. The main computational advantage of phase field models is that an explicit tracking of the interface is unnecessary. The regularized Dirac delta function is an important ingredient in many interfacial problems that phase field models have been applied. The delta function can be used to postprocess the phase field solution and represent the surface tension force. In this paper, we present and compare various types of delta functions for phase field models. In particular, we analytically show which type of delta function works relatively well regardless of whether an interfacial phase transition is compressed or stretched. Numerical experiments are presented to show the performance of each delta function. Numerical results indicate that (1) all of the considered delta functions have good performances when the phase field is locally equilibrated; and (2) a delta function, which is the absolute value of the gradient of the phase field, is the best in most of the numerical experiments. Copyright © 2012 John Wiley & Sons, Ltd.

Received 27 November 2010; Revised 27 September 2011; Accepted 28 November 2011

KEY WORDS: regularized Dirac delta function; phase field model; Cahn–Hilliard equation; Navier–Stokes equation

1. INTRODUCTION

Multiphase fluid flows are used in a wide variety of applications such as extractors [1], polymer-dispersed liquid crystals [2], polymer blends [3], reactors [4], separators [5], sprays [6], and microfluidic technology [7, 8]. The fluids with changes in the interface topology are complex with density, diffusivity, viscosity, and surface tension. The fluids play important roles in the transition process and affect both the post-transition structure of the flows and the dynamics of the transition itself. The transition typically results from the competition between flow instabilities (e.g., due to shear or density stratification) and stabilizing influences (e.g., due to surface tension and/or viscosity). For this reason, modeling and numerical simulation of multiphase fluid flows is a great challenge.

In simulating multiphase fluid flows, there are two main approaches: interface tracking and interface capturing. In interface tracking methods (front tracking [9, 10] and immersed boundary [11, 12]), Lagrangian particles are used to track the interface and are advected by the velocity field. In interface capturing methods (volume of fluid [VOF] [11, 13, 14], level set [15–18], and phase field [19–22]), the interface is implicitly captured by a contour of a particular scalar function. Many numerical techniques, including immersed boundary [23–30], VOF [31–40], and level set [41–48], use the concept of a regularized Dirac delta function to account for interfacial effects (this is described in more detail in Section 2), and many previous studies show that an appropriate delta function is required to obtain more accurate results. However, despite the large body of research on delta functions, the performance of delta functions for phase field models has not been clearly

^{*}Correspondence to: Junseok Kim, Department of Mathematics, Korea University, Seoul 136-701, Korea.

[†]E-mail: cfdkim@korea.ac.kr

addressed and compared. The purpose of this paper is to investigate the performance of regularized Dirac delta functions as a postprocessing of the phase field solution and a representation of the surface tension force for phase field models in interfacial flows undergoing topological transitions.

In a phase field model, the quantity $c(\mathbf{x}, t)$ is defined to be the mass concentration of one of the components. The Cahn–Hilliard (CH) equation was introduced to model spinodal decomposition and coarsening phenomena in binary alloys [49, 50]:

$$\frac{\partial c(\mathbf{x}, t)}{\partial t} = M \Delta \mu(c(\mathbf{x}, t)), \mathbf{x} \in \Omega, 0 < t \leq T, \quad (1)$$

$$\mu(c(\mathbf{x}, t)) = F'(c(\mathbf{x}, t)) - \epsilon^2 \Delta c(\mathbf{x}, t), \quad (2)$$

where $\Omega \subset \mathbf{R}^d$ ($d = 1, 2, 3$). The coefficient M represents a constant mobility. We set $M \equiv 1$ for convenience. This equation arises from the Ginzburg–Landau free energy

$$\mathcal{E}(c) := \int_{\Omega} \left(F(c) + \frac{\epsilon^2}{2} |\nabla c|^2 \right) d\mathbf{x}, \quad (3)$$

where $F(c)$ is the Helmholtz free energy and ϵ represents a positive constant. In this paper, the free energy is modeled by $F(c) = 0.25c^2(1 - c)^2$, which represents a double well potential with equilibrium values $c = 0$ and 1 (Figure 1). To obtain the CH equation, one introduces a chemical potential μ as the variational derivative of \mathcal{E} ,

$$\mu := \frac{\delta \mathcal{E}}{\delta c} = F'(c) - \epsilon^2 \Delta c,$$

and defines the flux, $\mathcal{J} := -M \nabla \mu$. As a consequence of mass conservation, we have

$$\frac{\partial c}{\partial t} = -\nabla \cdot \mathcal{J},$$

which is the CH equation. The natural and no-flux boundary conditions are

$$\frac{\partial c}{\partial \mathbf{n}} = \mathcal{J} \cdot \mathbf{n} = 0 \quad \text{on } \partial\Omega, \text{ where } \mathbf{n} \text{ is normal to } \partial\Omega.$$

We use an unconditionally gradient stable scheme [51–54] for solving Equations (1) and (2). The scheme is solved by an efficient and accurate nonlinear multigrid method. For a detailed description of the numerical solution, please refer to References [53, 55].

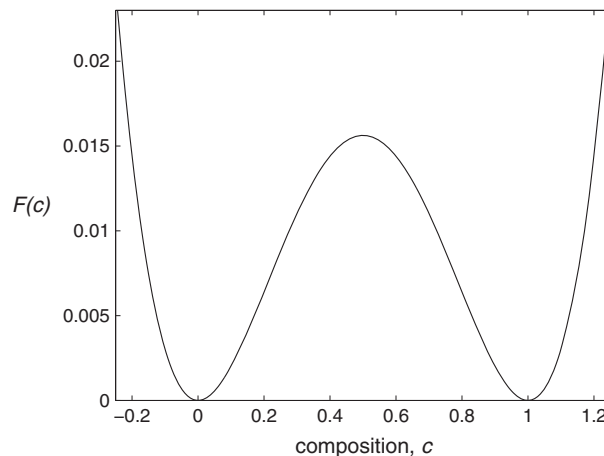


Figure 1. A double well potential, $F(c) = 0.25c^2(1 - c)^2$.

This paper is organized as follows. In Section 2, we review the numerical methods for regularized Dirac delta functions. We present various types of delta functions for phase field models and analyze feature of delta functions by the interface profile in Section 3. Numerical experiments are described in Section 4. In Section 5 conclusions are given.

2. REVIEW OF NUMERICAL METHODS FOR REGULARIZED DIRAC DELTA FUNCTIONS

We briefly review the numerical methods for regularized Dirac delta functions. Delta functions with immersed boundary [23–30], VOF [31–40], and level set [41–48] have been intensively studied.

2.1. Immersed boundary method

In the immersed boundary method, the elastic boundary is represented by a set of Lagrangian points, and the singular force at the Lagrangian points is determined by the generalized Hooke’s law. This force is spread to the surrounding Eulerian points using a delta function. In the immersed boundary method, most commonly used delta functions are 2-point [25, 28, 30], 3-point [27, 28, 30], 6-point [23, 24, 28, 29], 4-point cosine [26, 30], and 4-point [24, 26, 28, 30] functions. For all r , where r is the parameter representing the position of the submerged boundary point and is scaled with respect to the grid size h , the one-dimensional delta functions are listed as follows.

- 2-point delta function

$$\delta(r) = \begin{cases} 1 - |r| & \text{if } |r| \leq 1, \\ 0 & \text{otherwise.} \end{cases}$$

- 3-point delta function

$$\delta(r) = \begin{cases} \frac{1}{3} (1 + \sqrt{-3r^2 + 1}) & \text{if } |r| \leq 0.5, \\ \frac{1}{6} (5 - 3|r| - \sqrt{-3(1 - |r|)^2 + 1}) & \text{if } 0.5 \leq |r| \leq 1.5, \\ 0 & \text{otherwise.} \end{cases}$$

- 6-point delta function

$$\delta(r) = \begin{cases} \frac{61}{112} - \frac{11}{42}|r| - \frac{11}{56}|r|^2 + \frac{1}{12}|r|^3 + \frac{\sqrt{3}}{336} (243 + 1584|r| - 748|r|^2 - 1560|r|^3 + 500|r|^4 + 336|r|^5 - 112|r|^6)^{1/2} & \text{if } 0 \leq |r| \leq 1, \\ \frac{21}{16} + \frac{7}{12}|r| - \frac{7}{8}|r|^2 + \frac{1}{6}|r|^3 - \frac{3}{2}\delta(|r| - 1) & \text{if } 1 \leq |r| \leq 2, \\ \frac{9}{8} - \frac{23}{12}|r| + \frac{3}{4}|r|^2 - \frac{1}{12}|r|^3 + \frac{1}{2}\delta(|r| - 2) & \text{if } 2 \leq |r| \leq 3, \\ 0 & \text{otherwise.} \end{cases}$$

- 4-point cosine delta function

$$\delta(r) = \begin{cases} \frac{1}{4} (1 + \cos(\frac{\pi r}{2})) & \text{if } |r| \leq 2, \\ 0 & \text{otherwise.} \end{cases}$$

- 4-point delta function

$$\delta(r) = \begin{cases} \frac{1}{8} (3 - 2|r| + \sqrt{1 + 4|r| - 4r^2}) & \text{if } 0 \leq |r| \leq 1, \\ \frac{1}{8} (5 - 2|r| - \sqrt{-7 + 12|r| - 4r^2}) & \text{if } 1 \leq |r| \leq 2, \\ 0 & \text{otherwise.} \end{cases}$$

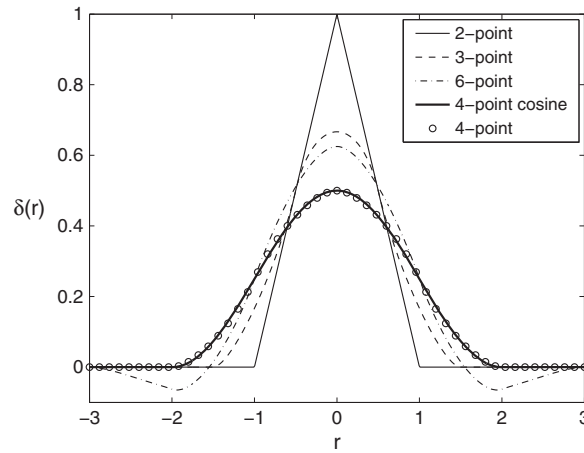


Figure 2. Five types of delta functions used in the immersed boundary method.

The aforementioned five types of delta functions are shown in Figure 2. Shin *et al.* [28] analyzed the stability regimes of the feedback forcing gains in the feedback forcing method for several types of delta functions and showed that non-growing oscillations became smaller for the delta function supported by more points. Yang *et al.* [30] found that the nonphysical oscillations are mainly because the derivatives of the regular discrete delta functions do not satisfy certain moment conditions and demonstrated that the smoothed discrete delta functions can effectively suppress the nonphysical oscillations in the volume forces and improve the accuracy of the immersed boundary method with direct forcing in moving boundary simulations.

2.2. Volume of fluid method

The VOF method was proposed by Hirt and Nichols [56]. In VOF method, the interface is reconstructed from the values of a color function that represents the volume fraction of one of the fluids in each cell. The continuum surface force (CSF) of Brackbill *et al.* [57] has been widely used to model surface tension in multiphase fluid flows in VOF method. In the CSF model [33, 34, 40, 58–61], the surface tension force is converted into a volume force via a delta function, $\mathbf{f} = \sigma\kappa\mathbf{n}\delta$, where σ is the surface tension coefficient, κ is the curvature, \mathbf{n} is the normal to the surface, and δ is a delta function. In VOF method, the most commonly used delta function is $\delta(\tilde{c}) = |\nabla\tilde{c}|$, where \tilde{c} is a smoothed version of the volume fraction. The CSF model is simple and robust, and it involves only the solving of a field equation for a smoothed phase field \tilde{c} . However, the method is known to produce strong and spurious currents near the interface. For this reason, many researchers have developed new methods to reduce spurious currents [37, 40, 62–64]. Meier *et al.* [37] reduced spurious currents using the piecewise-linear interface construction VOF method. In Reference [64], a parabolic reconstruction of surface tension algorithm is used to gain higher-order accuracy for the surface tension force.

2.3. Level set method

In the level set method, first devised and introduced by Osher and Sethian [65], delta functions are often used to distribute a singular force or to compute a surface area [46, 66–68]. Most commonly used delta functions are listed as follows. Here, ϵ is proportional to the grid size, that is, $\epsilon = mh$ for a positive number m .

- Delta function in References [41, 43, 45, 47, 48]

$$\delta_\epsilon(x) = \begin{cases} \frac{1}{\epsilon} \left(1 - \left|\frac{x}{\epsilon}\right|\right) & \text{if } |x| \leq \epsilon, \\ 0 & \text{otherwise.} \end{cases}$$

- Delta function in References [41–44, 46–48]

$$\delta_\epsilon(x) = \begin{cases} \frac{1}{2\epsilon} (1 + \cos(\frac{\pi x}{\epsilon})) & \text{if } |x| \leq \epsilon, \\ 0 & \text{otherwise.} \end{cases}$$

Tornberg and Engquist [69] pointed out that the most common technique for regularization of delta functions in level set simulations is not consistent and analyzed the accuracy of regularization of delta functions. Smereka [45] presented methods for constructing consistent approximations to Dirac delta measures concentrated on piecewise smooth curves or surfaces. Towers [70] proposed second-order finite difference methods for approximating Heaviside functions and showed that the methods are more accurate than a commonly used approximate Heaviside function.

3. REGULARIZED DIRAC DELTA FUNCTIONS FOR PHASE FIELD MODELS

In this section, we present eight types of delta functions for phase field models. From the Ginzburg–Landau free energy (3), the phase field c at the equilibrium state satisfies the following equation:

$$\frac{1}{4}c^2(1 - c)^2 = \frac{\epsilon^2}{2}|\nabla c|^2. \tag{4}$$

By using Equation (4) and delta functions used in phase field models [19, 21, 71–73], we get new delta functions for the present model. In this paper, eight types of delta functions are chosen:

- delta function in References [19, 71] $\delta_1(c) = 6\sqrt{2}\epsilon|\nabla c|^2$;
- new delta function $\delta_2(c) = 3\sqrt{2}c^2(1 - c)^2/\epsilon$;
- delta function in References [72, 73] $\delta_3(c) = 0.5(\delta_1(c) + \delta_2(c))$;
- delta function in Reference [21] $\delta_4(c) = 30\sqrt{2}\epsilon c(1 - c)|\nabla c|^2$;
- new delta function $\delta_5(c) = c(1 - c)/(\sqrt{2}\epsilon)$;
- new delta function $\delta_6(c) = |\nabla c|$;
- new delta function $\delta_7(c) = 0.5(\delta_5(c) + \delta_6(c))$; and
- new delta function $\delta_8(c) = 630\sqrt{2}\epsilon c^3(1 - c)^3|\nabla c|^2$.

For a flat interface with an equilibrium profile,

$$\int_{-\infty}^{\infty} \delta_i(c^{eq}) dx = 1 \quad \text{for all } i = 1, 2, \dots, 8,$$

where $c^{eq}(x, y) = 0.5(1 + \tanh(x/(2\sqrt{2}\epsilon)))$ is an equilibrium profile in the infinite domain when the chemical potential is given by Equation (2) [74], and it is a good approximation in the finite domain. Figure 3 shows delta functions used in this paper. We note that new delta functions $\delta_5(c)$ and $\delta_8(c)$ have wider and narrower supports than $\delta_1(c)$ and $\delta_4(c)$, respectively.

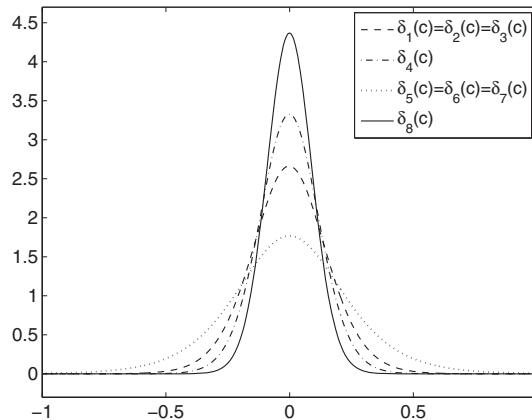


Figure 3. Delta functions for phase field models.

We now consider a line of unit length on a unit domain $\Omega = (0, 1) \times (0, 1)$:

$$c(x, y) = \frac{1}{2} \left(1 + \tanh \left(\frac{0.5 - x}{2\sqrt{2}a} \right) \right) \tag{5}$$

for different values of a . The value of a is related to the interface thickness. For $a = 0.5\epsilon, \epsilon$, and 2ϵ , the length of line is given by

$$f_i(a) = \int_{\Omega} \delta_i(c) \, dx \, dy.$$

This integral is calculated using the Mathematica (Wolfram Research, Inc., Champaign, IL, USA) code given in Appendix A. The results are given in Table I. Next, we consider a circle of radius 0.25 at the center of a domain $\Omega = (0, 1) \times (0, 1)$:

$$c(x, y) = \frac{1}{2} \left(1 + \tanh \left(\frac{0.25 - \sqrt{(x - 0.5)^2 + (y - 0.5)^2}}{2\sqrt{2}a} \right) \right).$$

The circumference for the different values of a is given in Table I. In both cases, $\delta_6(c)$ is insensitive to the value of a . This means that the length of line or circle can be computed accurately using $\delta_6(c)$ regardless of the interface thickness. We will numerically discuss this in more details in Section 4. Figure 4 shows the graphs of $f_i(a)$ for $i = 1, 2, \dots, 8$.

Table I. The length of line and circle with different interface thicknesses for each delta function.

	Case 1: line			Case 2: circle			$f_i(a)$
	a			a			
	0.5ϵ	ϵ	2ϵ	0.5ϵ	ϵ	2ϵ	
δ_1	2	1	0.5	π	0.5π	0.25π	$f_1(a) = 1/a$
δ_2	0.5	1	2	0.25π	0.5π	π	$f_2(a) = a$
δ_3	1.25	1	1.25	0.625π	0.5π	0.625π	$f_3(a) = (1/a + a)/2$
δ_4	2	1	0.5	π	0.5π	0.25π	$f_4(a) = 1/a$
δ_5	0.5	1	2	0.25π	0.5π	π	$f_5(a) = a$
δ_6	1	1	1	0.5π	0.5π	0.5π	$f_6(a) = 1$
δ_7	0.75	1	1.5	0.375π	0.5π	0.75π	$f_7(a) = (a + 1)/2$
δ_8	2	1	0.5	π	0.5π	0.25π	$f_8(a) = 1/a$

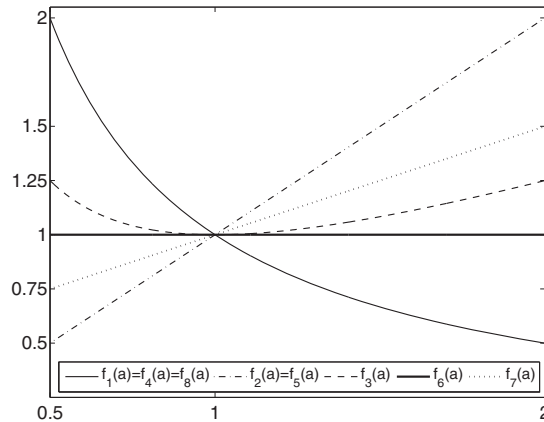


Figure 4. The graphs of $f_i(a)$ for $i = 1, 2, \dots, 8$.

4. NUMERICAL EXPERIMENTS

We now present numerical results to show the performance of regularized Dirac delta functions as (1) a postprocessing of the phase field solution, that is, length of line and circle, Rayleigh–Taylor instability, deformation of a circle by a single vortex, a three-dimensional deformation field, and triply periodic minimal surfaces (TPMS); and (2) a representation of the surface tension force, that is, reduction of spurious velocities and pressure jump across the drop. And we also demonstrate relation between the interfacial width and grid size. Across the interfacial region, the concentration field varies from 0.1 to 0.9 over a distance of approximately $4\sqrt{2}\epsilon \tanh^{-1}(0.8)$. Therefore, if we want this value to be approximately $m (> 0)$ grid points, the ϵ value needs to be taken as $\epsilon_m = hm / [4\sqrt{2} \tanh^{-1}(0.8)]$. Figure 5 shows the concentration $c(x) = 0.5 \left(1 + \tanh \left(x / (2\sqrt{2}\epsilon_m) \right) \right)$ with $m = 4, 8, 12,$ and 16 . We will use various ϵ that is suitable for each problem.

4.1. The Dirac delta function as a postprocessing of the phase field solution

In this section, we investigate the performance of each delta function as an interface length or a surface area calculation tool. The interface length \mathcal{L} and surface area \mathcal{A} are defined as

$$\mathcal{L}(c) = \sum_{i=1}^{N_x} \sum_{j=1}^{N_y} \delta(c_{ij})h^2 \quad \text{and} \quad \mathcal{A}(c) = \sum_{i=1}^{N_x} \sum_{j=1}^{N_y} \sum_{k=1}^{N_z} \delta(c_{ijk})h^3,$$

where $N_x, N_y,$ and N_z are the number of grid points in the $x, y,$ and z directions, respectively. The discrete composition field c_{ij} (or c_{ijk}) is located at cell centers, and h is the uniform mesh size.

When there is no theoretical value of an interface length or a surface area, we need a reasonable value corresponding to the theoretical value. To obtain a reasonable value, we take the initial condition as

$$c(x, y, 0) = \frac{1}{2} \left(1 + \tanh \left(\frac{0.25 - \sqrt{(x - 0.5)^2 + (y - 0.5)^2}}{2\sqrt{2}\epsilon_4} \right) \right)$$

on the computational domain $\Omega = (0, 1) \times (0, 1)$, which represents a circle with a radius 0.25. We calculate the length of a 0.5-level contour using MATLAB (The MathWorks, Inc., Natick, MA, USA). The results with increasingly finer grids are given in Table II.

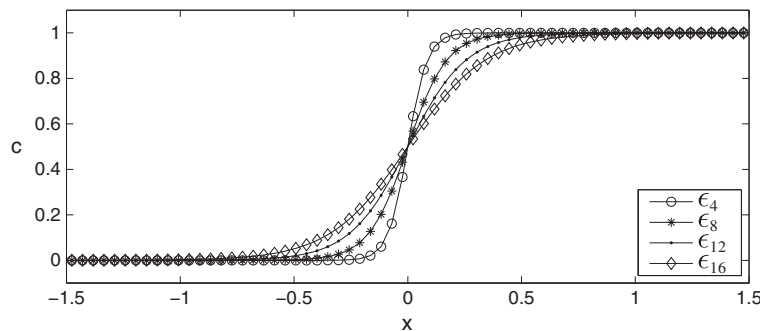


Figure 5. The concentration $c(x) = 0.5(1 + \tanh(x/(2\sqrt{2}\epsilon_m)))$ with $m = 4, 8, 12,$ and 16 .

Table II. Comparison between the theoretical value and the length of contour.

Mesh	16^2	32^2	64^2	128^2	Theoretical value
Interface length	1.565632	1.569770	1.570572	1.570778	$2\pi r \approx 1.570796$

Table III. Comparison between the theoretical value and the area of isosurface.

Mesh	32 ³	64 ³	128 ³	256 ³	Theoretical value
Surface area	0.781695	0.784493	0.785185	0.785364	4πr ² ≈ 0.785398

Next, the initial condition is

$$c(x, y, z, 0) = \frac{1}{2} \left(1 + \tanh \left(\frac{0.25 - \sqrt{(x - 0.5)^2 + (y - 0.5)^2 + (z - 0.5)^2}}{2\sqrt{2}\epsilon_4} \right) \right)$$

on $\Omega = (0, 1) \times (0, 1) \times (0, 1)$, which represents a sphere with a radius 0.25. We compute the area of an isosurface by summation of the areas of all triangle tiles in the isosurface using MATLAB. The results with increasingly finer grids are given in Table III. The results in Tables II and III suggest that the length of contour and the area of isosurface agree well with the theoretical value.

4.1.1. *Test 1: length of line and circle.* In Section 3, we explored the performance of delta functions by the interface profile using Mathematica. To numerically explore the performance, we consider two initial conditions on $\Omega = (0, 1) \times (0, 1)$:

$$c(x, y, 0) = \frac{1}{2} \left(1 + \tanh \left(\frac{0.5 - x}{2\sqrt{2}a} \right) \right) \quad \text{and}$$

$$c(x, y, 0) = \frac{1}{2} \left(1 + \tanh \left(\frac{0.25 - \sqrt{(x - 0.5)^2 + (y - 0.5)^2}}{2\sqrt{2}a} \right) \right)$$

for $a = 0.5\epsilon_8, \epsilon_8$, and $2\epsilon_8$. We choose $h = 1/128$ and $\Delta t = 10h$.

Figures 6(a)–(c) (case of line) and 7(a)–(c) (case of circle) show the contour lines of concentration with $a = 0.5\epsilon_8, \epsilon_8$, and $2\epsilon_8$, respectively. The length of line and circle for each delta function is given in Table IV. From Table IV, it is observed that δ_6 accurately calculates the length of line and circle regardless of whether an interface transition is compressed ($a = 0.5\epsilon_8$) or stretched ($a = 2\epsilon_8$). Figures 6(d) and 7(d) show the percentage error of each delta function of cases of line and circle by representing them as histograms of various sizes, respectively.

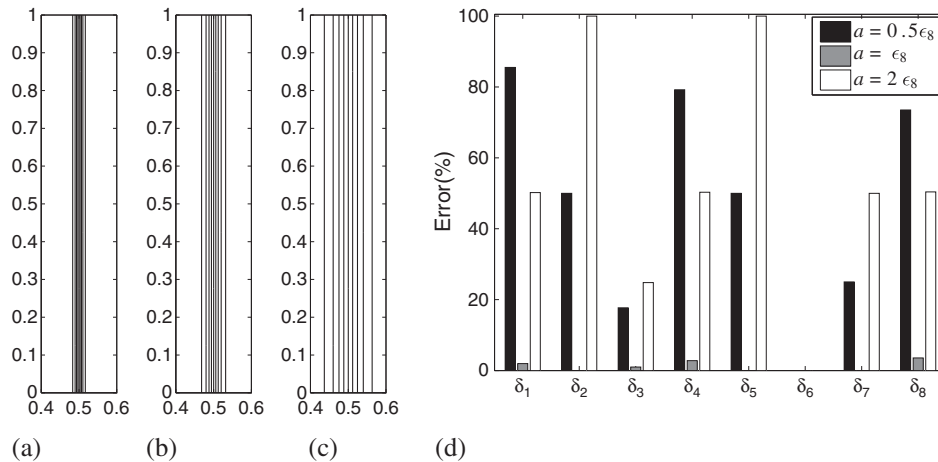


Figure 6. The length of line. The contour lines of concentration with (a) $a = 0.5\epsilon_8$, (b) $a = \epsilon_8$, and (c) $a = 2\epsilon_8$. Contour levels are 0.1, 0.2, ..., 0.9. (d) The percentage error of each delta function.

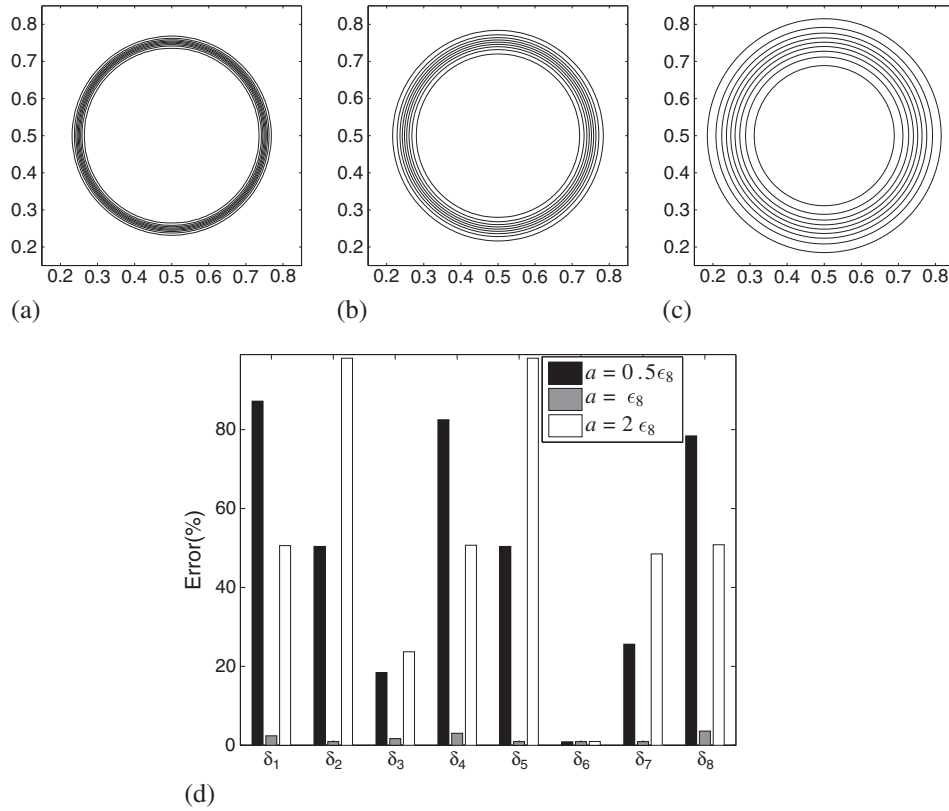


Figure 7. The length of circle. The contour lines of concentration with (a) $a = 0.5\epsilon_8$, (b) $a = \epsilon_8$, and (c) $a = 2\epsilon_8$. Contour levels are 0.1, 0.2, . . . , 0.9. (d) The percentage error of each delta function.

Table IV. The length of line and circle for each delta function.

Case	a	Contour value	δ_1	δ_2	δ_3	δ_4	δ_5	δ_6	δ_7	δ_8
Line	$0.5\epsilon_8$	1.0000	1.8556	0.5000	1.1778	1.7929	0.5000	1.0000	0.7500	1.7353
	ϵ_8	1.0000	0.9804	1.0000	0.9902	0.9720	1.0000	1.0000	1.0000	0.9645
	$2\epsilon_8$	1.0000	0.4975	2.0000	1.2488	0.4964	2.0000	1.0000	1.5000	0.4955
Circle	$0.5\epsilon_8$	1.5849	2.9677	0.7854	1.8766	2.8927	0.7854	1.5708	1.1781	2.8278
	ϵ_8	1.5855	1.5473	1.5708	1.5590	1.5373	1.5708	1.5706	1.5707	1.5284
	$2\epsilon_8$	1.5857	0.7823	3.1416	1.9619	0.7810	3.1413	1.5704	2.3558	0.7799

4.1.2. *Test 2: Rayleigh–Taylor instability.* When a heavy fluid is superposed over a light fluid in a gravitational field, the fluid interface is unstable. Any perturbation of this interface tends to grow with time, producing the phenomenon known as the Rayleigh–Taylor instability. This phenomenon represents the penetration of both heavy and light fluids into each other. The Rayleigh–Taylor instability for a fluid in a gravitational field was originally introduced by Rayleigh [75] and later applied to all accelerated fluids by Taylor [76]. In order to simulate the Rayleigh–Taylor instability, the Navier–Stokes–Cahn–Hilliard equations (NSCH) are preferred. The NSCH equations can be written in a dimensionless form

$$\rho(c)(\mathbf{u}_t + \mathbf{u} \cdot \nabla \mathbf{u}) = -\nabla p + \frac{1}{Re} \Delta \mathbf{u} + \frac{\rho(c)}{Fr} \mathbf{g},$$

$$\nabla \cdot \mathbf{u} = 0,$$

$$c_t + \nabla \cdot (c\mathbf{u}) = \frac{1}{Pe} \Delta \mu,$$

$$\mu = f(c) - C \Delta c,$$

where \mathbf{u} is the velocity, p is the pressure, $\rho(c) = \rho_1 c + \rho_2(1 - c)$ is the variable density (ρ_1 and ρ_2 are the densities of the heavier and lighter fluid, respectively), and $\mathbf{g} = (0, -1)$. The dimensionless parameters are the Reynolds number, $Re = \rho_* U_* L_* / \eta$, Froude number, $Fr = U_*^2 / (g L_*)$, Peclet number, $Pe = U_* L_* / (M \mu_*)$, and Cahn number, $C = \epsilon^2 / (\mu_* L_*^2)$. The values with lower $*$ are characteristic values of corresponding ones, η is the viscosity, and g is the acceleration due to gravity. Here, the effect of the surface tension is negligible. For a detailed description of the numerical method used in solving the NSCH equations, please refer to Reference [77].

We calculate the length of the interface with three different Peclet numbers. The initial condition is

$$c(x, y, 0) = \frac{1}{2} \left(1 + \tanh \left(\frac{y - 2 - 0.1 \cos(2\pi x)}{2\sqrt{2}\epsilon} \right) \right)$$

on $\Omega = (0, 1) \times (0, 4)$, which represents a planar interface superimposed by a perturbation of wave number $k = 1$ and amplitude 0.1. The density ratio is $\rho_1 : \rho_2 = 3 : 1$, and we use the simulation parameters such as the uniform grids $h = 1/128$, $\Delta t = 0.00125$, $\epsilon = 0.01$, and $Re = 3000$.

Figure 8(a) shows the evolution of the interface with $Pe = 1/\epsilon$ at times $t = 0, 1$, and 2. The results are given in Table V. In the numerical simulations of the Rayleigh–Taylor instability, as the Pe number increases, the width of an interface transition becomes nonuniform (Figures 8(b)–(d)). As a result, the percentage error of almost all delta functions is high (Figure 9). But, the result obtained using δ_6 is in better agreement with the contour value, regardless of the Pe number.

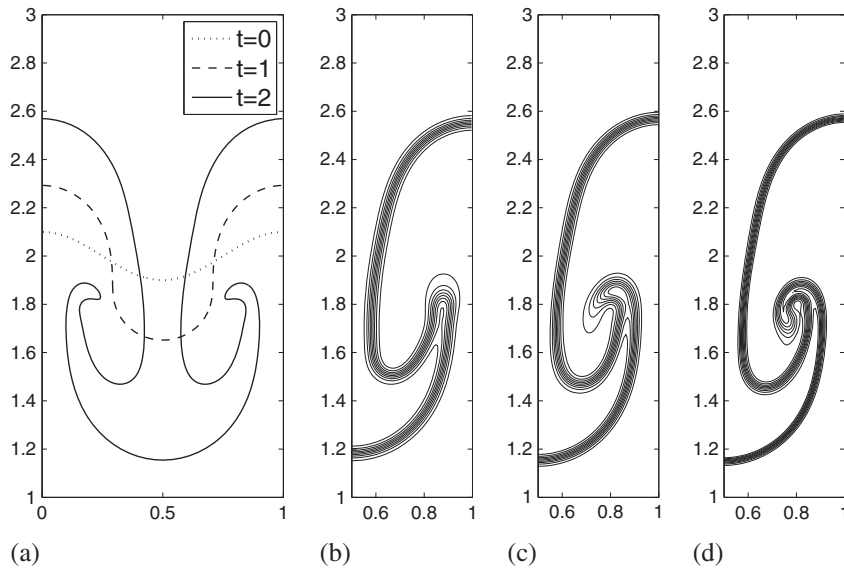


Figure 8. (a) The evolution of the interface with $Pe = 1/\epsilon$ at times $t = 0, 1$, and 2. The effect of the Peclet number on the temporal evolution of the interface at time $t = 2$: (b) $Pe = 0.1/\epsilon$, (c) $Pe = 1/\epsilon$, and (d) $Pe = 10/\epsilon$. Contour levels are 0.1, 0.2, ..., 0.9.

Table V. Rayleigh–Taylor instability: the interface length for each delta function.

Pe	Contour value	δ_1	δ_2	δ_3	δ_4	δ_5	δ_6	δ_7	δ_8
$0.1/\epsilon$	5.169	4.955	5.478	5.217	4.953	5.798	5.097	5.447	4.950
$1/\epsilon$	5.832	6.385	5.532	5.958	6.222	4.611	5.924	5.267	6.150
$10/\epsilon$	6.455	10.38	4.387	7.386	9.596	2.974	6.901	4.938	9.328

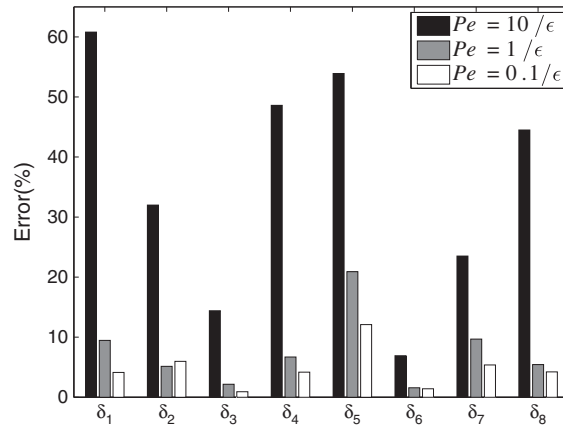


Figure 9. Rayleigh–Taylor instability: the percentage error of each delta function.

4.1.3. *Test 3: deformation of a circle by a single vortex.* In this test, a circle is deformed with a velocity field defined by $u = k \sin^2(\pi x) \sin(2\pi y)$ and $v = -k \sin(2\pi x) \sin^2(\pi y)$. In order to demonstrate the capability of each delta function in an extreme velocity field, we choose $k = 100$, which is much larger than values used in the previous experiments. This flow satisfies $u = v = 0$ on the boundaries of the unit square domain. As shown in Figure 10(a) by the dotted line, initially, the circle has a radius of 0.15 and is centered at (0.50, 0.75) in the unit square domain. The phase field is initialized to $c = 1$ and $c = 0$ inside and outside the circle, respectively. The advection by the vorticity field causes the circle to evolve into a filament that spirals toward the vortex center at (0.5, 0.5). The numerical solutions are computed on the uniform grids $h = 1/128$, and the calculation is run with $\Delta t = 0.00125/k$ and $\epsilon = 0.01$. Figure 10(a) shows the evolution of the interface at times $t = 0, 0.0025$, and 0.005. The results are given in Table VI. For most of delta functions, except δ_6 , the error is large because of the compressed interfacial transition (Figure 10(b)). But, as seen in Section 3, δ_6 yields a good result even though the interfacial transition is compressed (Figure 10(c)).

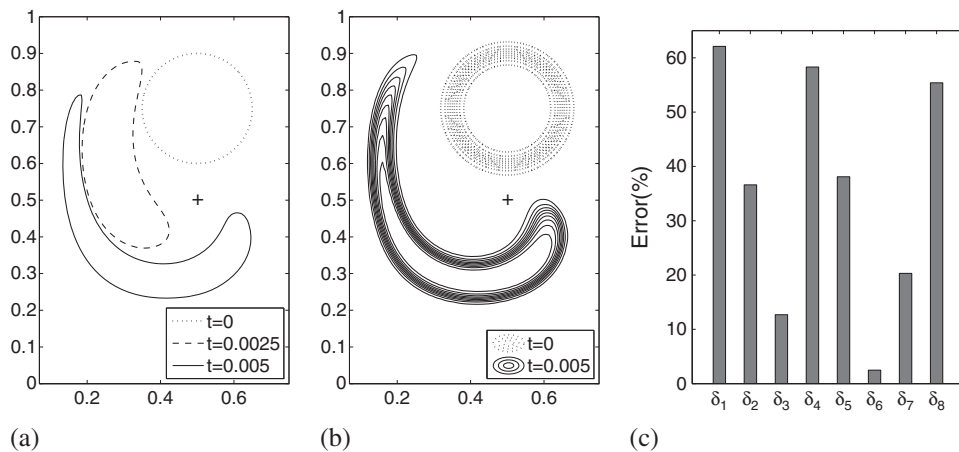


Figure 10. (a) The evolution of the interface at times $t = 0, 0.0025$, and 0.005. (b) Contour lines of concentration. Contour levels are 0.1, 0.2, . . . , 0.9. (c) The percentage error of each delta function.

Table VI. Deformed circle: the interface length for each delta function.

Contour value	δ_1	δ_2	δ_3	δ_4	δ_5	δ_6	δ_7	δ_8
1.968	3.192	1.246	2.219	3.117	1.218	1.919	1.568	3.060

4.1.4. *Test 4: three-dimensional deformation field.* We consider the problem of a deforming sphere in a velocity field given by $u = 2 \sin^2(\pi x) \sin(2\pi y) \sin(2\pi z)$, $v = -\sin(2\pi x) \sin^2(\pi y) \sin(2\pi z)$, and $w = -\sin(2\pi x) \sin(2\pi y) \sin^2(\pi z)$ [78]. A simulation of this problem has previously been performed by Enright *et al.* using the level set method [79]. This flow satisfies $u = v = w = 0$ on the boundaries of the unit cube domain. A sphere of radius 0.15 is placed within a unit computational domain at (0.35, 0.35, 0.35). We take $h = 1/256$, $\Delta t = 2.5e-4$, ϵ_3 , and $Pe = 0.1/\epsilon_3$.

Figure 11 shows the evolution of the interface at times $t = 0, 0.2, 0.4$, and 0.6 . Each figure can be compared with the figures from the level set computation in Reference [79]. The sphere is entrained by two rotating vortices and then is compressed into a pancake-like shape. The surface of the pancake-like shape becomes stretched out. Parts of the interface thin out to about a few grid, and almost all delta functions have difficulty to calculate exactly the surface area of this thin interface (see the results in Table VII). But, δ_6 has very little error even if the surface is deformed. Figure 12 shows the percentage error of each delta function by representing them as histograms of various sizes.

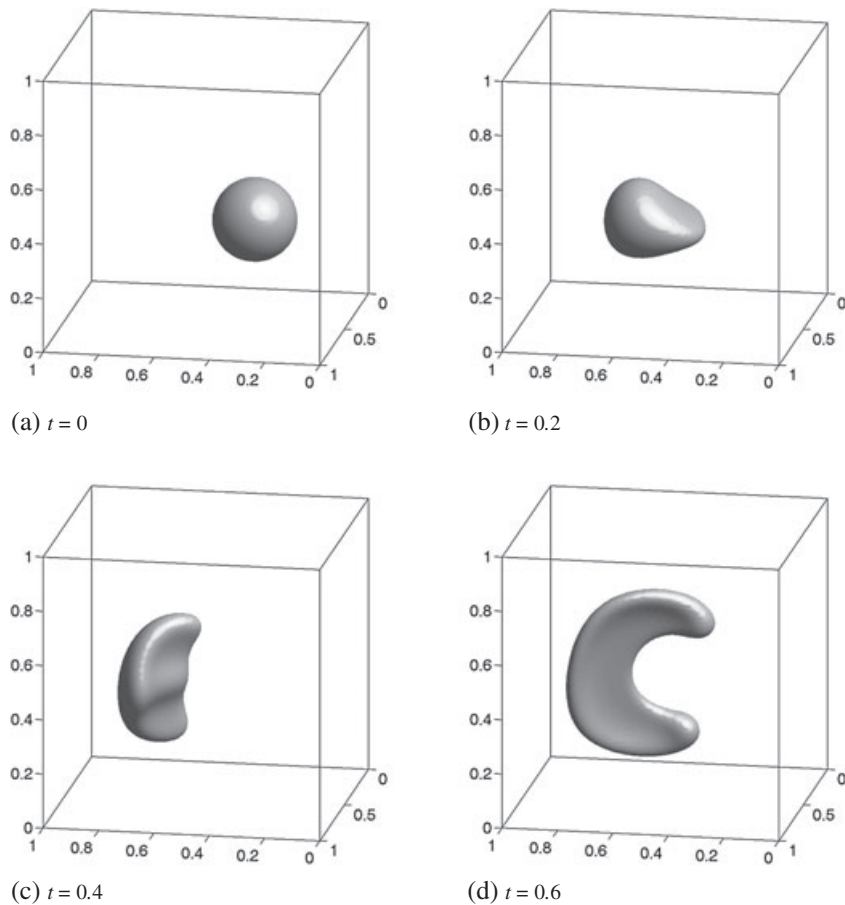


Figure 11. Deformation test: the evolution of the interface. (a) $t = 0$, (b) $t = 0.2$, (c) $t = 0.4$, and (d) $t = 0.6$.

Table VII. Deformed sphere: the surface area for each delta function.

Isosurface value	δ_1	δ_2	δ_3	δ_4	δ_5	δ_6	δ_7	δ_8
0.586	0.565	0.567	0.566	0.545	0.634	0.596	0.615	0.528

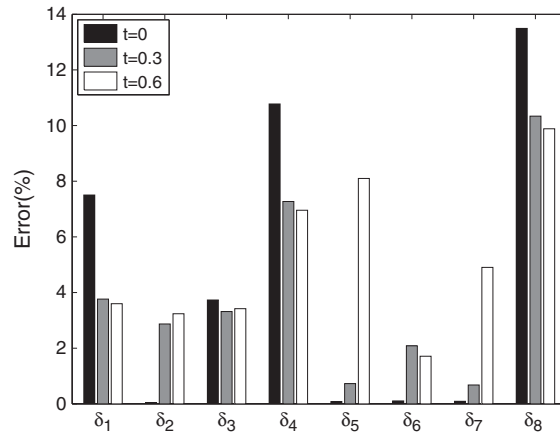


Figure 12. Deformed sphere: the percentage error of each delta function.

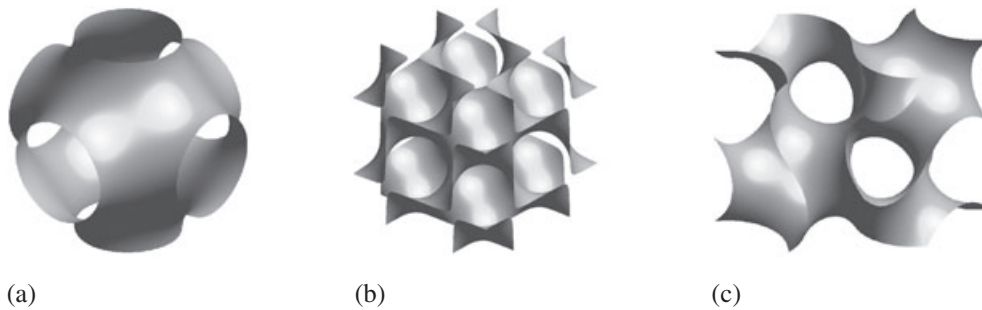


Figure 13. Triply periodic minimal surfaces: (a) Schwarz primitive, (b) Schwarz diamond, and (c) Schoen gyroid.

4.1.5. *Test 5: triply periodic minimal surfaces.* Triply periodic minimal surfaces (Figure 13) are of special interest because they appear in a variety of real structures such as silicates, bicontinuous mixtures, lyotropic colloids, detergent films, lipid bilayers, and biological formations [80]. One important application of TPMS is tissue scaffolds. Tissue scaffolds should have an optimal surface area and pore size to restore function or regenerate tissue more efficiently. The TPMS morphology has been successfully adapted to tissue scaffolds [81]. To calculate surface areas of TPMS, we take the periodic nodal surface approximations of the primitive (P), diamond (D), and gyroid (G) TPMS [82]:

$$\begin{aligned}
 P(x, y, z) &= \cos 2\pi x + \cos 2\pi y + \cos 2\pi z + 0.5, \\
 D(x, y, z) &= \cos 2\pi x \cos 2\pi y \cos 2\pi z - \sin 2\pi x \sin 2\pi y \sin 2\pi z + 0.5, \\
 G(x, y, z) &= \sin 2\pi x \cos 2\pi y + \sin 2\pi z \cos 2\pi x + \sin 2\pi y \cos 2\pi z + 0.5.
 \end{aligned}$$

For these calculations, we employ the computational domain $\Omega = (0, 1) \times (0, 1) \times (0, 1)$ with $h = 1/256$, $\Delta t = 0.5h$, and $\epsilon = 0.01$. We stop the numerical computations when the discrete l_2 -norm of the difference between $(n + 1)$ th and n th time step solutions becomes less than 10^{-6} . That is, $\|c^{n+1} - c^n\| \leq 10^{-6}$. In Table VIII, we compare surface areas obtained using each delta function with those obtained by Jung *et al.* [83]. As we can see from Figure 14, the error of δ_6 is small.

4.2. *The Dirac delta function in the surface tension force formulation*

An accurate approximation of the surface tension force is essential for solving two-phase incompressible fluid flows. The CSF model of Brackbill *et al.* [57] is employed extensively to model the surface tension force of two-phase incompressible fluid flows in VOF [32, 61, 64, 84], level

Table VIII. TPMS: the surface area for each delta function.

TPMS [‡]	δ_1	δ_2	δ_3	δ_4	δ_5	δ_6	δ_7	δ_8
P surface (2.34)	2.21	2.24	2.22	2.11	2.29	2.35	2.32	2.02
D surface (3.84)	3.57	3.63	3.60	3.39	3.80	3.82	3.81	3.22
G surface (3.10)	2.88	2.93	2.91	2.74	3.14	3.08	3.11	2.60

[‡]From the results in Reference [83].

TPMS, triply periodic minimal surfaces; P, primitive; D, diamond; G, gyroid.

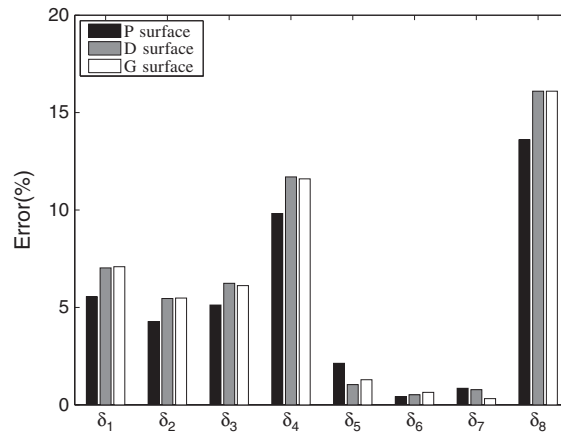


Figure 14. Triply periodic minimal surfaces: the percentage error of each delta function. P, primitive; D, diamond; G, gyroid.

set [46, 59], and phase field [19–21, 58, 60] methods. In the CSF model, surface tension forces acting on the interface are transformed to volume forces in regions near the interface via a delta function, $\mathbf{SF} = \sigma\kappa\delta\mathbf{n}$, where σ is the surface tension coefficient, κ is the curvature, δ is a delta function concentrated on the interface, and \mathbf{n} is the unit outward normal to the surface and defined by $\mathbf{n} = \nabla c / |\nabla c|$. We note the identity

$$\nabla \cdot \mathbf{n} = -\kappa. \quad (6)$$

For a derivation of Equation (6), see Reference [57]. The governing equations for two-phase incompressible fluid flows can be written as [19–21]

$$\begin{aligned} \rho(\mathbf{u}_t + \mathbf{u} \cdot \nabla \mathbf{u}) &= -\nabla p + \eta \Delta \mathbf{u} - \sigma \nabla \cdot \left(\frac{\nabla c}{|\nabla c|} \right) \delta(c) \frac{\nabla c}{|\nabla c|}, \\ \nabla \cdot \mathbf{u} &= 0, \\ c_t + \nabla \cdot (c\mathbf{u}) &= M \Delta \mu, \\ \mu &= f(c) - \epsilon^2 \Delta c. \end{aligned} \quad (7)$$

For details of the numerical solution, we refer to Reference [19]. In this section, we present two tests for the surface tension force.

4.2.1. Reduction of spurious velocities. Spurious or parasitic velocities are unphysical currents that arise from a slight imbalance between stresses in the interfacial region. There are a number of papers for spurious velocities in incompressible flow problems [35, 85–88]. Approximating and choosing the surface tension force formulation accurately is important because an improper formulation will lead to spurious velocities. In this section, we compare the performance of each delta function with the similar test problem in Reference [64]. The computational domain is $\Omega = (0, 1) \times (0, 1)$, and the time step is $\Delta t = 10^{-5}$. The boundary conditions are zero velocity at the top and bottom walls, and periodicity in x -direction. Initially, a circular drop is centered at $(0.5, 0.5)$, with radius $a = 0.1$

and surface tension coefficient $\sigma = 0.357$. Both fluids have equal density, 4, and viscosity, 1. The initial velocity field is zero. The exact solution is zero velocity for all time. In dimensionless terms, the relevant parameter is the Ohnesorge number $Oh = \eta / \sqrt{\sigma \rho a} \sim 2.6463$.

Table IX shows the convergence of spurious velocities as we refine the mesh size for each delta function. Most delta functions show minor decreases as we refine the mesh. But, δ_1 , δ_6 , and δ_7 show a linear convergence of spurious velocities, and δ_6 effectively eliminates spurious velocities than δ_1 and δ_7 . In Figure 15, scaled velocity vector plots at 200th time step with $\Delta t = 10^{-5}$ are shown. These show the locations of spurious velocities with mesh refinement, (a) $h = 1/64$, (b) $1/128$, and (c) $1/256$ with $\epsilon = 0.64h$. Spurious velocities are mainly concentrated in the neighborhood of the interface. The convergence of spurious velocities is evident as we refine the mesh size h and interface parameter ϵ .

4.2.2. *Pressure jump across the drop.* Let us consider the equilibrium of a drop placed within another fluid. Let the drop composition be defined as

$$c(x, y) = \frac{1}{2} \left(1 + \tanh \left(\frac{0.1 - \sqrt{(x - 0.5)^2 + (y - 0.5)^2}}{2\sqrt{2}\epsilon} \right) \right).$$

In the equilibrium state of a droplet, the velocity vanishes ($\mathbf{u} \equiv 0$) and therefore Equation (7) reduces to Equation (8) and therefore pressure gradient should balance surface tension force.

$$\nabla p = -\sigma \nabla \cdot \left(\frac{\nabla c}{|\nabla c|} \right) \delta(c) \frac{\nabla c}{|\nabla c|}. \tag{8}$$

We solve Equation (9) numerically by taking the divergence operator to Equation (8) with $\sigma = 20$, 128×128 mesh, computational domain $\Omega = (0, 1) \times (0, 1)$, and $\epsilon = 0.005$.

$$\Delta p = -\sigma \nabla \cdot \left[\nabla \cdot \left(\frac{\nabla c}{|\nabla c|} \right) \delta(c) \frac{\nabla c}{|\nabla c|} \right]. \tag{9}$$

Table IX. l_2 -norm of velocity at 200th time step with $\epsilon = 0.64h$ and $\Delta t = 10^{-5}$.

Case	δ_1	δ_2	δ_3	δ_4	δ_5	δ_6	δ_7	δ_8
64^2	2.064e-5	4.460e-5	3.219e-5	3.010e-5	3.019e-5	2.232e-5	2.599e-5	4.463e-5
128^2	1.112e-5	4.345e-5	2.663e-5	1.901e-5	1.820e-5	1.018e-5	1.389e-5	2.667e-5
256^2	5.880e-6	4.264e-5	2.350e-5	1.325e-5	1.318e-5	4.653e-6	8.362e-6	2.137e-5

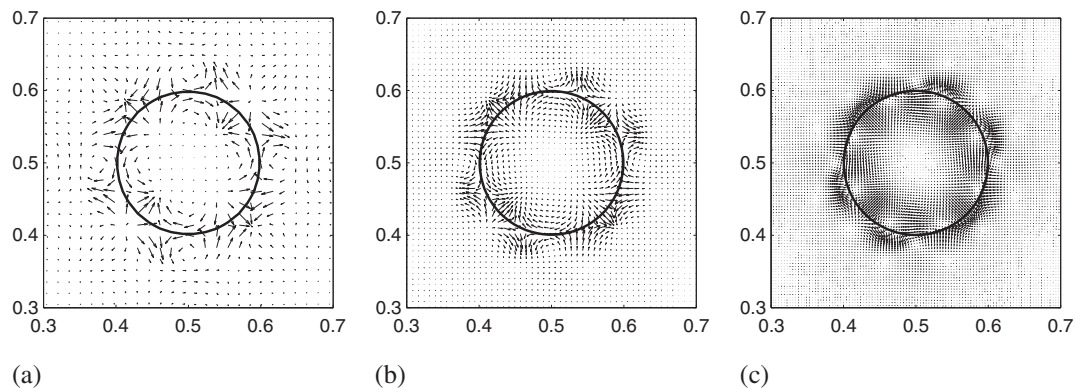


Figure 15. Scaled velocity vector plots at 200th time step with $\Delta t = 10^{-5}$. These show the locations of spurious velocities with mesh refinement, (a) $h = 1/64$, (b) $h = 1/128$, and (c) $h = 1/256$ with $\epsilon = 0.64h$. The solid line in each figure represents the interface. The length of the arrow is proportional to the magnitude of the velocity vector.

Table X. The numerical pressure jump $[p]$ across the drop with $\sigma = 20$ and $R = 0.1$.

Case	δ_1	δ_2	δ_3	δ_4	δ_5	δ_6	δ_7	δ_8
$[p]$	190.40	199.08	194.58	182.76	197.31	199.70	198.48	176.90

From Laplace's formulation, we can obtain the theoretical prediction of the pressure jump inside an infinite cylinder as $\Delta p_{\text{theo}} = \sigma/R$, where R is the drop radius. In this test, the pressure jump Δp_{theo} is 200. This value is compared with the difference between the maximum and the minimum computed drop pressures obtained with each delta function, $[p]$, defined as

$$[p] = \max_{i,j} p_{ij} - \min_{i,j} p_{ij}.$$

As shown in Table X, the numerical pressure jump $[p]$ obtained using δ_6 is in excellent agreement with the theoretical prediction.

4.3. Relation between the interfacial width and grid size

With the mass conserving boundary condition ($\nabla \mu \cdot \mathbf{n} = 0$ on $\partial\Omega$), the differentiation of the total mass yields

$$\frac{d}{dt} \int_{\Omega} \phi \, d\mathbf{x} = \int_{\Omega} \phi_t \, d\mathbf{x} = \int_{\Omega} \Delta \mu \, d\mathbf{x} = \int_{\partial\Omega} \nabla \mu \cdot \mathbf{n} \, ds = 0, \quad (10)$$

where ϕ is the phase field variable, and we redefine ϕ as the difference between the concentration of the two components. Equation (10) means that the solution of the CH equation conserves mass over the entire domain. Even though the phase field variable is conserved globally, the mass of a drop is liable to variations as the ϕ evolves. Theoretically, such variations vanish as the interfacial thickness approaches zero. But, in practice, the interfacial thickness is finite. This was pointed out by Yue *et al.* [73]. To minimize the variations of mass, Yue *et al.* provided the guidelines on how to pick the interfacial width and grid size relative to the radius of curvature. And the authors calculated the shift of the phase field variable and found that the shift $\delta\phi$ is proportional to ϵ/r_0 , where r_0 is the initial drop radius.

In this section, we perform numerical simulations of the spontaneous shrinking of a drop. A drop with initial radius $r_0 = 0.75$ and interfacial width $\epsilon_{8,3281}$ (this value corresponds to the value in Section 2.2 in Reference [73]) and ϵ_{30} is simulated. The initial drop is at the center of the computational domain $\Omega = (-2, 2) \times (-2, 2)$, and a 128×128 mesh is used. Figure 16(a),(b) shows the phase field ϕ at $y = 0$ for $\epsilon_{8,3281}$ and ϵ_{30} , respectively. In the case of $\epsilon_{8,3281}$, a grid size h is $\epsilon_{8,3281}/2$, and a 128×128 mesh is sufficient to guarantee numerical accuracy. Thus, we can see that ϕ at the

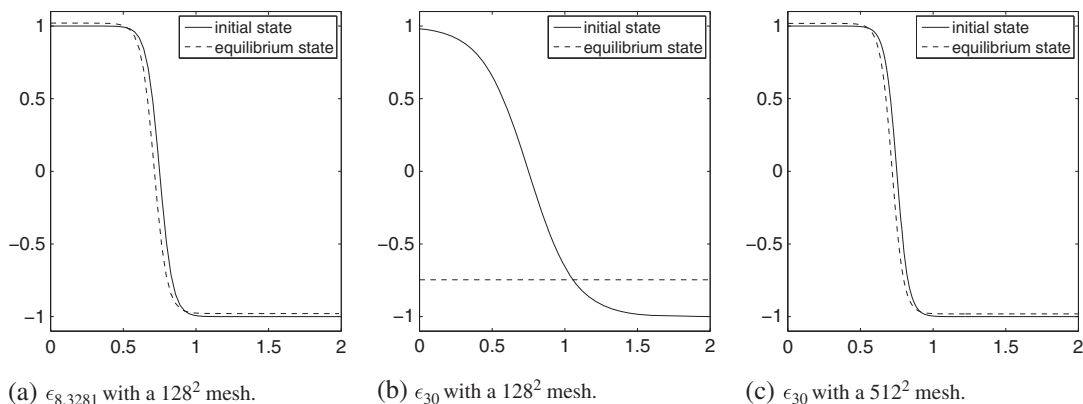


Figure 16. Each figure shows the phase field at $y = 0$. The interfacial width and grid size for each case are as follows: (a) $\epsilon_{8,3281}$ with a 128^2 mesh, (b) ϵ_{30} with a 128^2 mesh, and (c) ϵ_{30} with a 512^2 mesh.

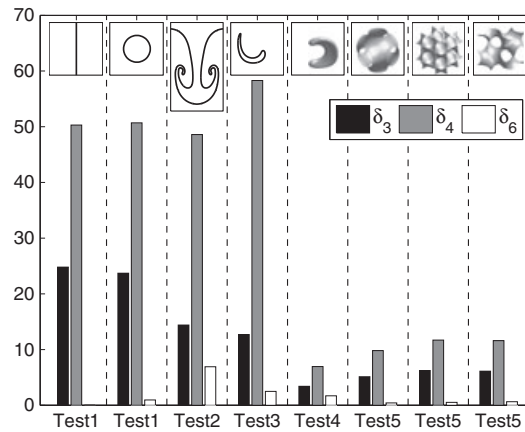


Figure 17. Schematic illustration of the results of the five tests in Section 4.1.

equilibrium state shifts slightly away from the initial state. But, in the case of ϵ_{30} , a 128×128 mesh is too coarse compared with that in $\epsilon_{8.3281}$. As a result, the phase field disperses (Figure 16(b)). In Figure 16(c), we use a 512×512 mesh with ϵ_{30} and obtain a more accurate result than the result in Figure 16(b). Therefore, to guarantee numerical accuracy, we need to choose properly an interfacial width and grid size.

5. CONCLUSION

In this paper, we presented and compared various types of delta functions for phase field models. In particular, we analytically showed which type of delta function works relatively well regardless of whether an interfacial phase transition is compressed or stretched. Numerical experiments were presented to show the performance of each delta function as a postprocessing of the phase field solution and a representation of the surface tension force. Figure 17 summarizes the results of Section 4.1. Numerical results indicated that (1) all of the considered delta functions have good performances when the phase field is locally equilibrated; and (2) a delta function, which is the absolute value of the gradient of the phase field, is the best in most of the numerical experiments.

APPENDIX A:

In this section, we present a Mathematica code to calculate the integral of regularized Dirac delta functions.

```
e=0.1; a=e; Inf=Infinity;
f[x_]=0.5(1+Tanh[(0.5-x)/(2Sqrt[2]a)]);
g[x_]=D[f[x],x];
d1=NIntegrate[(6Sqrt[2]e)g[x]^2,{x,-Inf,Inf}]
d2=NIntegrate[(3Sqrt[2])(f[x](1-f[x]))^2/e,{x,-Inf,Inf}]
d3=(d1+d2)/2
d4=NIntegrate[(30Sqrt[2]e)f[x](1-f[x])g[x]^2,{x,-Inf,Inf}]
d5=NIntegrate[f[x](1-f[x])/(Sqrt[2]e),{x,-Inf,Inf}]
d6=NIntegrate[Abs[g[x]},{x,-Inf,Inf}]
d7=(d5+d6)/2
d8=NIntegrate[(630Sqrt[2]e)(f[x](1-f[x]))^3g[x]^2,{x,-Inf,Inf}]
```

ACKNOWLEDGEMENTS

This research was supported by Basic Science Research Program through the National Research Foundation of Korea (NRF), funded by the Ministry of Education, Science and Technology (No. 2011-0023794). The authors also wish to thank the reviewers for their constructive and helpful comments on the revision of this article.

REFERENCES

1. Rieger R, Weiss C, Wigley G, Bart H-J, Marr R. Investigating the process of liquid-liquid extraction by means of computational fluid dynamics. *Computers & Chemical Engineering* 1996; **20**:1467–1475.
2. West JL. *Polymer-dispersed liquid crystals*, Liquid-Crystalline Polymers Chap. 32, 1990.
3. Tucker CL, Moldenaers P. Microstructural evolution in polymer blends. *The Annual Review of Fluid Mechanics* 2002; **34**:177–210.
4. Sundaresan S. Modeling the hydrodynamics of multiphase flow reactors: current status and challenges. *AIChE Journal* 2000; **46**:1102–1105.
5. Crowe CT, Sommerfeld M, Tsuji Y. *Multiphase Flows with Droplets and Particles*. CRC Press: Florida, 1998.
6. Dukowicz JK. A particle-fluid numerical model for liquid sprays. *Journal of Computational Physics* 1980; **35**:229–253.
7. Ménétrier-Deremble L, Tabeling P. Droplet breakup in microfluidic junctions of arbitrary angles. *Physical Review E* 2006; **74**:035303-1–035303-4.
8. De Menech M. Modeling of droplet breakup in a microfluidic T-shaped junction with a phase-field model. *Physical Review E* 2006; **73**:031505-1–031505-9.
9. Tryggvason G, Bunner B, Esmaeeli A, Juric D, Al-Rawahi N, Tauber W, Han J, Nas S, Jan Y-J. A front-tracking method for the computations of multiphase flow. *Journal of Computational Physics* 2001; **169**:708–759.
10. Unverdi SO, Tryggvason G. A front-tracking method for viscous, incompressible, multi-fluid flows. *Journal of Computational Physics* 1992; **100**:25–37.
11. Pederzani J, Haj-Hariri H. A numerical method for the analysis of flexible bodies in unsteady viscous flows. *International Journal for Numerical Methods in Engineering* 2006; **68**:1096–1112.
12. Udaykumar HS, Kan H-C, Shyy W, Tran-Son-Tay R. Multiphase dynamics in arbitrary geometries on fixed cartesian grids. *Journal of Computational Physics* 1997; **137**:366–405.
13. Kietzmann CvL, Van Der Walt JP, Morsi YS. A free-front tracking algorithm for a control-volume-based Hele-Shaw method. *International Journal for Numerical Methods in Engineering* 1998; **41**:253–269.
14. Mehdi-Nejad V, Mostaghimi J, Chandra S. Modelling heat transfer in two-fluid interfacial flows. *International Journal for Numerical Methods in Engineering* 2004; **61**:1028–1048.
15. Battaglia L, Storti MA, D'Elia J. Bounded renormalization with continuous penalization for level set interface-capturing methods. *International Journal for Numerical Methods in Engineering* 2010; **84**:830–848.
16. Challis VJ, Guest JK. Level set topology optimization of fluids in Stokes flow. *International Journal for Numerical Methods in Engineering* 2009; **79**:1284–1308.
17. Gómez P, Hernández J, López J. On the reinitialization procedure in a narrow-band locally refined level set method for interfacial flows. *International Journal for Numerical Methods in Engineering* 2005; **63**:1478–1512.
18. Sochnikov V, Efrima S. Level set calculations of the evolution of boundaries on a dynamically adaptive grid. *International Journal for Numerical Methods in Engineering* 2003; **56**:1913–1929.
19. Kim J. A continuous surface tension force formulation for diffuse-interface models. *Journal of Computational Physics* 2005; **204**:784–804.
20. Kim J. Phase field computations for ternary fluid flows. *Computer Methods in Applied Mechanics and Engineering* 2007; **196**:4779–4788.
21. Kim J. A generalized continuous surface tension force formulation for phase-field models for multi-component immiscible fluid flows. *Computer Methods in Applied Mechanics and Engineering* 2009; **198**:3105–3112.
22. Yue P, Feng JJ, Liu C, Shen J. A diffuse-interface method for simulating two-phase flows of complex fluids. *The Journal of Fluid Mechanics* 2004; **515**:293–317.
23. Griffith BE, Hornung RD, McQueen DM, Peskin CS. An adaptive, formally second order accurate version of the immersed boundary method. *Journal of Computational Physics* 2007; **223**:10–49.
24. Griffith BE, Peskin CS. On the order of accuracy of the immersed boundary method: Higher order convergence rates for sufficiently smooth problems. *Journal of Computational Physics* 2005; **208**:75–105.
25. LeVeque RJ, Li Z. The immersed interface method for elliptic equations with discontinuous coefficients and singular sources. *SIAM Journal on Numerical Analysis* 1994; **31**:1019–1044.
26. Peskin CS. The immersed boundary method. *Acta Numerica* 2002; **11**:479–517.
27. Roma AM, Peskin CS, Berger MJ. An adaptive version of the immersed boundary method. *Journal of Computational Physics* 1999; **153**:509–534.
28. Shin SJ, Huang W-X, Sung HJ. Assessment of regularized delta functions and feedback forcing schemes for an immersed boundary method. *International Journal for Numerical Methods in Fluids* 2008; **58**:263–286.
29. Stockie JM. Analysis and computation of immersed boundaries, with application to pulp fibres. *Ph.D. thesis*, Institute of Applied Mathematics, University of British Columbia, 1997.

30. Yang X, Zhang X, Li Z, He G-W. A smoothing technique for discrete delta functions with application to immersed boundary method in moving boundary simulations. *Journal of Computational Physics* 2009; **228**:7821–7836.
31. Chen L, Li Y. A numerical method for two-phase flows with an interface. *Environmental Modelling & Software* 1998; **13**:247–255.
32. Coward AV, Renardy YY, Renardy M, Richards JR. Temporal evolution of periodic disturbances in two-layer Couette flow. *Journal of Computational Physics* 1997; **132**:346–361.
33. Gao D, Morley NB, Dhir V. Numerical simulation of wavy falling film flow using VOF method. *Journal of Computational Physics* 2003; **192**:624–642.
34. Gueyffier D, Li J, Nadim A, Scardovelli R, Zaleski S. Volume-of-fluid interface tracking with smoothed surface stress methods for three-dimensional flows. *Journal of Computational Physics* 1999; **152**:423–456.
35. Lafaurie B, Nardone C, Scardovelli R, Zaleski S, Zanetti G. Modelling merging and fragmentation in multiphase flows with SURFER. *Journal of Computational Physics* 1994; **113**:134–147.
36. Lörstad D, Fuchs L. High-order surface tension VOF-model for 3D bubble flows with high density ratio. *Journal of Computational Physics* 2004; **200**:153–176.
37. Meier M, Yadigaroglu G, Smith BL. A novel technique for including surface tension in PLIC-VOF methods. *European Journal of Mechanics - B/Fluids* 2002; **21**:61–73.
38. Rudman M. A volume-tracking method for incompressible multifluid flows with large density variations. *International Journal for Numerical Methods in Fluids* 1998; **28**:357–378.
39. Scardovelli R, Zaleski S. Direct numerical simulation of free-surface and interfacial flow. *The Annual Review of Fluid Mechanics* 1999; **31**:567–603.
40. Tang H, Wrobel LC, Fan Z. Tracking of immiscible interfaces in multiple-material mixing processes. *Computational Materials Science* 2004; **29**:103–118.
41. Engquist B, Tornberg A-K, Tsai R. Discretization of dirac delta functions in level set methods. *Journal of Computational Physics* 2005; **207**:28–51.
42. Jin S, Wen X. Hamiltonian-preserving schemes for the Liouville equation with discontinuous potentials. *Communications in Mathematical Sciences* 2005; **3**:285–315.
43. Jin S, Liu H, Osher S, Tsai Y-HR. Computing multivalued physical observables for the semiclassical limit of the Schrödinger equation. *Journal of Computational Physics* 2005; **205**:222–241.
44. Jin S, Liu H, Osher S, Tsai Y-HR. Computing multi-valued physical observables for high frequency limit of symmetric hyperbolic systems. *Journal of Computational Physics* 2005; **210**:497–518.
45. Smereka P. The numerical approximation of a delta function with application to level set methods. *Journal of Computational Physics* 2006; **211**:77–90.
46. Sussman M, Smereka P, Osher S. A level set method for computing solutions to incompressible two-phase flow. *Journal of Computational Physics* 1994; **114**:146–159.
47. Towers JD. Two methods for discretizing a delta function supported on a level set. *Journal of Computational Physics* 2007; **220**:915–931.
48. Wen X. High order numerical methods to a type of delta function integrals. *Journal of Computational Physics* 2007; **226**:1952–1967.
49. Cahn JW. On spinodal decomposition. *Acta Metallurgica* 1961; **9**:795–801.
50. Cahn JW, Hilliard JE. Free energy of a nonuniform system. I. Interfacial free energy. *Journal of Chemical Physics* 1958; **28**:258–267.
51. Eyre D J. An Unconditionally Stable One-Step Scheme for Gradient Systems. <http://www.math.utah.edu/~eyre/research/methods/stable.ps>.
52. Eyre DJ. *Computational and Mathematical Models of Microstructural Evolution*. The Material Research Society: Pennsylvania, 1998.
53. Kim J, Bae H-O. An unconditionally stable adaptive mesh refinement for Cahn–Hilliard equation. *Journal of the Korean Physical Society* 2008; **53**:672–679.
54. Vollmayr-Lee BP, Rutenberg AD. Fast and accurate coarsening simulation with an unconditionally stable time step. *Physical Review E* 2003; **68**:066703-1–066703-13.
55. Kim J. A numerical method for the Cahn–Hilliard equation with a variable mobility. *Communications in Nonlinear Science and Numerical Simulation* 2007; **12**:1560–1571.
56. Hirt CW, Nichols BD. Volume of fluid (VOF) method for the dynamics of free boundaries. *Journal of Computational Physics* 1981; **39**:201–225.
57. Brackbill JU, Kothe DB, Zemach C. A continuum method for modelling surface tension. *Journal of Computational Physics* 1992; **100**:335–354.
58. Badalassi VE, Cenicer HD, Banerjee S. Computation of multiphase systems with phase field models. *Journal of Computational Physics* 2003; **190**:371–397.
59. Chang YC, Hou TY, Merriman B, Osher S. A level set formulation of Eulerian interface capturing methods for incompressible fluid flows. *Journal of Computational Physics* 1996; **124**:449–464.
60. Chella R. Mixing of a two-phase fluid by cavity flow. *Physical Review E* 1996; **53**:3832–3840.
61. Renardy YY, Renardy M, Cristini V. A new volume-of-fluid method for surfactants and simulations of drop deformation under shear at a low viscosity ratio. *European Journal of Mechanics - B/Fluids* 2002; **21**:49–59.
62. Khismatullin D, Renardy YY, Renardy M. Development and implementation of VOF-PROST for 3D viscoelastic liquid. liquid simulations. *Journal of Non-Newtonian Fluid Mechanics* 2006; **140**:120–131.

63. Pilliod Jr. JE, Puckett EG. Second-order volume-of-fluid algorithms for tracking material interfaces. *Journal of Computational Physics* 2004; **199**:465–502.
64. Renardy YY, Renardy M. PROST: a parabolic reconstruction of surface tension for the volume-of-fluid method. *Journal of Computational Physics* 2002; **183**:400–421.
65. Osher S, Sethian J. Fronts propagating with curvature-dependent speed: algorithms based on Hamilton-Jacobi formulations. *Journal of Computational Physics* 1988; **79**:12–49.
66. Hou TY, Li Z, Osher S, Zhao H. A hybrid method for moving interface problems with application to the Hele-Shaw flow. *Journal of Computational Physics* 1997; **134**:236–252.
67. Liu X-D, Fedkiw RP, Kang M. A boundary condition capturing method for Poisson's equation on irregular domains. *Journal of Computational Physics* 2000; **160**:151–178.
68. Peng D, Merriman B, Osher S, Zhao H, Kang M. A PDE-based fast local level set method. *Journal of Computational Physics* 1990; **155**:410–438.
69. Tornberg A-K, Engquist B. Numerical approximations of singular source terms in differential equations. *Journal of Computational Physics* 2004; **200**:462–488.
70. Towers JD. Finite difference methods for approximating Heaviside functions. *Journal of Computational Physics* 2009; **228**:3478–3489.
71. Yang S-D, Lee HG, Kim J. A phase-field approach for minimizing the area of triply periodic surfaces with volume constraint. *Computer Physics Communications* 2010; **181**:1037–1046.
72. Wang X. Phase field models and simulations of vesicle bio-membranes. *Ph.D. thesis*, Department of Mathematics, Penn State University, 2005.
73. Yue P, Zhou C, Feng JJ. Spontaneous shrinkage of drops and mass conservation in phase-field simulations. *Journal of Computational Physics* 2007; **223**:1–9.
74. Jacqmin D. Contact-line dynamics of a diffuse fluid interface. *The Journal of Fluid Mechanics* 2000; **402**:57–88.
75. Rayleigh L. Investigation of the character of the equilibrium of an incompressible heavy fluid of variable density. *Proceedings of the London Mathematical Society* 1883; **14**:170–177.
76. Taylor G. The instability of liquid surfaces when accelerated in a direction perpendicular to their planes. I. *Proceedings of the Royal Society of London A* 1950; **201**:192–196.
77. Lee HG, Kim K, Kim J. On the long time simulation of the Rayleigh–Taylor instability. *International Journal for Numerical Methods in Engineering* 2011; **85**:1633–1647.
78. LeVeque R. High-resolution conservative algorithms for advection in incompressible flow. *SIAM Journal on Numerical Analysis* 1996; **33**:627–665.
79. Enright D, Fedkiw R, Ferziger J, Mitchell I. A hybrid particle level set method for improved interface capturing. *Journal of Computational Physics* 2002; **183**:83–116.
80. Hyde S, Andersson S, Larsson K, Blum Z, Landh T, Lidin S, Ninham BW. *The Language of Shape: The Role of Curvature in Condensed Matter: Physics, Chemistry and Biology*. Elsevier Science: Amsterdam, 1997.
81. Rajagopalan S, Robb RA. Schwarz meets Schwann: design and fabrication of biomorphic and durataxic tissue engineering scaffolds. *Medical Image Analysis* 2006; **10**:693–712.
82. Von Schnering HG, Nesper R. Nodal surfaces of Fourier series: fundamental invariants of structured matter. *Zeitschrift für Physik B Condensed Matter* 1991; **83**:407–412.
83. Jung Y, Chu KT, Torquato S. A variational level set approach for surface area minimization of triply-periodic surfaces. *Journal of Computational Physics* 2007; **223**:711–730.
84. Rider WJ, Kothe D. Reconstructing volume tracking. *Journal of Computational Physics* 1998; **141**:112–152.
85. Ganesan S, Matthies G, Tobiska L. On spurious velocities in incompressible flow problems with interfaces. *Computer Methods in Applied Mechanics and Engineering* 2007; **196**:1193–1202.
86. Gerbeau J-F, Le Bris C, Bercovier M. Spurious velocities in the steady flow of an incompressible fluid subjected to external forces. *International Journal for Numerical Methods in Fluids* 1997; **25**:679–695.
87. Gresho P, Lee R, Chan S, Leone JA. A new finite element for incompressible or Boussinesq fluids. *Proceedings of the Third International Conference on Finite Elements in Flow Problems*, Banff, Canada, 1980.
88. Pelletier D, Fortin A, Camarero R. Are FEM solutions of incompressible flows really incompressible? (Or how simple flows can cause headaches!). *International Journal for Numerical Methods in Fluids* 1989; **9**:99–112.